MATERIALS SCIENCE

Massively parallel microwire arrays integrated with CMOS chips for neural recording

Abdulmalik Obaid[1]*, Mina-Elraheb Hanna[1,2]*, Yu-Wei Wu[3]*, Mihaly Kollo[4,5]*, Romeo Racz[4], Matthew R. Angle[2], Jan Müller[6], Nora Brackbill[7], William Wray[4], Felix Franke[6], E. J. Chichilnisky[8], Andreas Hierlemann[6], Jun B. Ding[3], Andreas T. Schaefer[4,5†‡], Nicholas A. Melosh[1†‡]

Multi-channel electrical recordings of neural activity in the brain is an increasingly powerful method revealing new aspects of neural communication, computation, and prosthetics. However, while planar silicon-based CMOS devices in conventional electronics scale rapidly, neural interface devices have not kept pace. Here, we present a new strategy to interface silicon-based chips with three-dimensional microwire arrays, providing the link between rapidly-developing electronics and high density neural interfaces. The system consists of a bundle of microwires mated to large-scale microelectrode arrays, such as camera chips. This system has excellent recording performance, demonstrated via single unit and local-field potential recordings in isolated retina and in the motor cortex or striatum of awake moving mice. The modular design enables a variety of microwire types and sizes to be integrated with different types of pixel arrays, connecting the rapid progress of commercial multiplexing, digitisation and data acquisition hardware together with a three-dimensional neural interface.

INTRODUCTION

Neural activity occurs within interconnected populations of neurons operating over a range of length scales and spatial locations throughout the brain. Recording sufficient numbers of neurons at natural time scales and spatial distributions is one of the foremost challenges for improved understanding of how neuronal ensembles operate in different behavioral states (*1*, *2*). Optical methods are increasingly used in studies of network dynamics in vivo, as they permit the monitoring of activity over a large area from the same layer of brain tissue (*3*–*5*). While improving, current optical techniques are limited in sampling rate, obscuring fine temporal patterns that have been found to carry substantial information in neuronal population codes (*6*). Furthermore, they are inherently limited to recording from superficial structures or require the use of, e.g., microendoscope probes or surgical resection of overlying tissue to provide access to deeper brain regions (*7*, *8*).

A number of innovations have been made for electrical recording using flexible materials on the surface of the brain, and planar probes have seen rapid development based on silicon processing techniques (*9*, *10*). However, recording from volumetrically distributed sites at scale has remained challenging due to the inherently two-dimensional nature of these devices. Since many brain areas (e.g., neocortex, hippocampus, and olfactory bulb) are organized in strata, sampling broad horizontal layers over large areas would be highly beneficial, as demonstrated by imaging experiments (*11*).

Microelectrodes and Si microarrays [Utah arrays (*12*)] have long been the standard for high-speed, distributed recording electrodes, yet are limited in channel count due to connectorization, volumetric displacement, and tissue damage. At the same time, complementary metal-oxide semiconductor (CMOS)–based electronics continues to evolve at a rapid pace for slice and culture recordings (*13*–*15*), yet few of these technological improvements make their way to in vivo neuroscience (*16*). Apart from individual electrodes, scaling has been frustrated by the engineering challenge for connectors, amplification, and digitization with integrated active electronics (*10*), posing noise and temperature challenges (*17*).

Here, we report a new strategy to take advantage of the scalability and electronic processing power of CMOS-based devices combined with a three-dimensional neural interface. The core concept is shown in Fig. 1A and further described in Kollo *et al.* (*18*), consisting of a bundle of insulated microwires perpendicularly mated to a large-scale CMOS amplifier array, such as a pixel array found in commercial camera or display chips. While microwires have low insertion damage and excellent electrical recording performance (*19*–*21*), they have been difficult to scale because they require individual mounting and connectorization (*22*, *23*). By arranging them into bundles, we control the spatial arrangement and three-dimensional structure of the distal (neuronal) end, with a robust parallel contact plane on the proximal side mated to a planar pixel array.

This architecture provides an array of microwires over the brain surface, akin to a Utah array (*12*), rather than along a single recording plane, such as with Si or polymer shank probes. Moreover, the insertion depth of the microelectrodes can be shaped to accommodate specific spatial distributions. The modular nature of the design allows a wide array of microwire types and size to be mated to different CMOS chips. The density of the microwires for the proximal (chip) end (Fig. 1B) and the distal (brain) end (Fig. 1C) can be modulated independently (fig. S3H), allowing the wire-to-wire spacing to be tailored as desired. The same fundamental platform is scalable from a few hundred to tens of thousands of electrodes, with electronic capabilities for both recording and stimulation. We thus link the rapid progress and power of commercial CMOS multiplexing, digitization,

[1]Department of Materials Science and Engineering, Stanford University, Stanford, CA, USA. [2]Paradromics Inc., Austin, TX, USA. [3]Department of Neurosurgery, Stanford University School of Medicine, Stanford, CA, USA. [4]Neurophysiology of Behaviour Laboratory, Francis Crick Institute, London, UK. [5]Department of Neuroscience, Physiology and Pharmacology, University College London, London, UK. [6]Department of Biosystems Science and Engineering, ETH Zurich, Basel, Switzerland. [7]Department of Physics, Stanford University, Stanford, CA, USA. [8]Departments of Neurosurgery and Ophthalmology, Stanford University, Stanford, CA, USA.
*These authors contributed equally to this work.
†These authors share senior authorship.
‡Corresponding author. Email: nmelosh@stanford.edu (N.A.M.); andreas.schaefer@crick.ac.uk (A.T.S.)

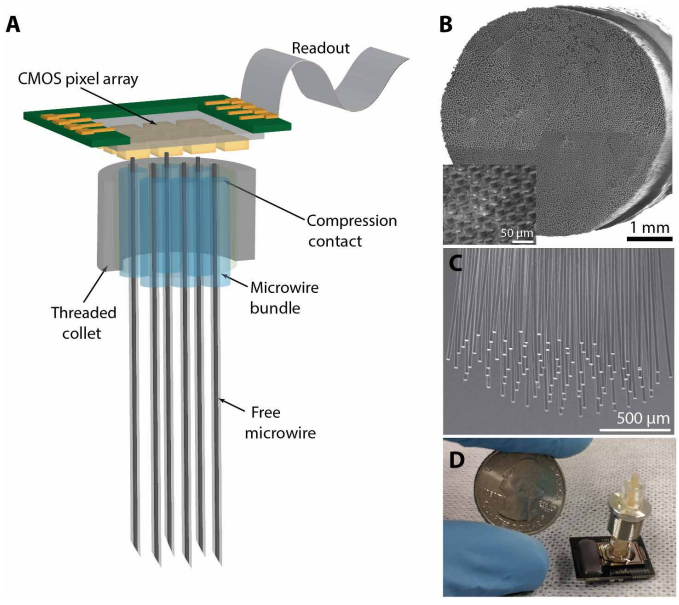

Fig. 1. Neural bundle design. (**A**) Schematic of the CMOS chip integrated with the microwire bundle. The bundle consists of a proximal (chip) end (**B**) designed for contact to the CMOS pixels, and a distal (brain) end (**C**) designed to record in tissue. The proximal end has partially exposed metal wires to contact the chip, while the distal end wires are separated to limit tissue damage upon insertion. (**D**) A bundle of 800 microwires spaced 100 µm apart, with a device form factor less than 0.6 cm wide appropriate for small-animal studies. Photo credit: Mina Hanna, Stanford University.

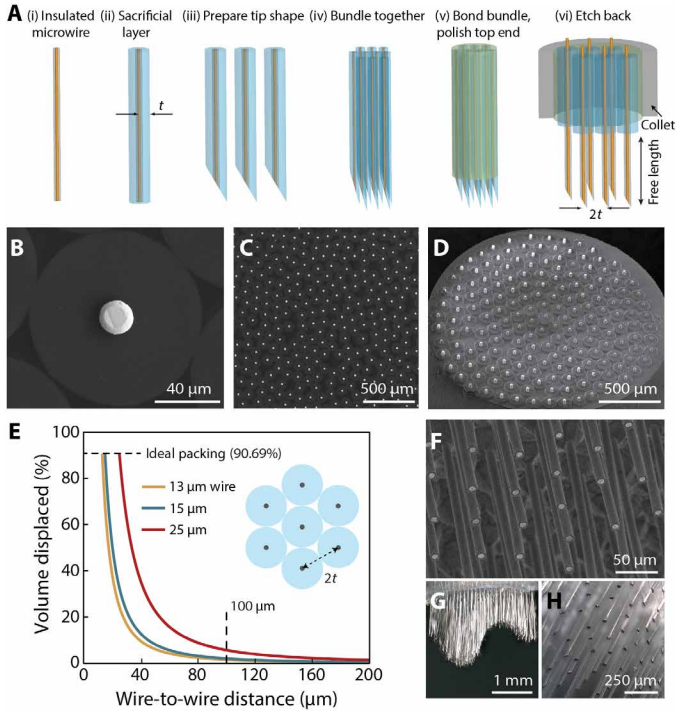

Fig. 2. Microwire bundle fabrication. (**A**) Fabrication procedure of microwire bundles. (i) Individual microwires are electrically insulated with a robust ceramic or polymeric coating. (ii) A sacrificial layer of parylene-C (PaC) is coated onto the wires to provide spacing. (iii) If desired, the tips of the microwires can be polished to an angular tip or electrosharpened. (iv) The wires are then bundled together by either spooling the wire or mechanical aggregation. The wires naturally pack in a honeycomb array. (v) The bundle is infiltrated with biomedical epoxy to hold the wires together and then the top (proximal) end is polished for mating to the CMOS chip. (vi) The proximal end is etched 10 to 20 µm to mate to the CMOS chip and the distal end of the wires is released by etching with oxygen plasma, allowing each wire to penetrate individually. A threaded collet is added to hold the bundle. (**B**) A backscatter SEM of an individual microwire with a PtIr conductive core and 45-µm PaC coating (A, ii). (**C**) Wires pack into a honeycomb structure, and epoxy is infiltrated in between to fill the gaps (A, v). (**D**) Proximal end of a bundle of 177 20-µm Au wires with 100-µm spacing after etching to expose the conductive wire. (**E**) Predicted volumetric displacement of bundles of microwires as a function of wire-to-wire distance, determined by the wire size and sacrificial coating thickness (*t*). This assumes a perfect hexagonal packing fraction of ~90.69%. For 15-µm wires with 100-µm spacing, the volume displaced is 2%. (**F**) The distal end of a bundle of 600 7.5-µm W wires coated with 1 µm of glass after etching to remove the PaC and embedded epoxy. (**G** and **H**) The distal end (PtW 20-µm wires, 100-µm spacing) can be shaped with single wire precision to simultaneously access different depths in the tissue.

and data acquisition hardware together with a biocompatible, flexible, and sensitive neural interface array.

RESULTS AND DISCUSSION

Microwire bundles

The microwire bundle fabrication design is shown in Fig. 2A, enabling different wire core and insulating materials, wire-to-wire spacing, and tip shape to be created (fig. S3, E and F). The central concept is to bundle together insulated microwires using a sacrificial coating on each one to define the wire-to-wire separation. Insulated microwires were prepared either by depositing a glass or polymer coating or by thermally drawing a glass/metal wire (*18*, *24*, *25*). We demonstrate bundles made with metal wires of diameters 5 to 25 µm and wire materials including Au, W, PtIr, and PtW. In principle, this strategy should be applicable to virtually any wire material or size. The high conductivity of metals allows for ultrathin metal cores (down to <1 µm), with an adjustable insulating layer from <1 to >50 µm thick. In typical preparations, the bare metal wire was wrapped around an open 10-cm spindle, followed by depositing a glass insulating layer ~1 µm thick using silane decomposition in a Thermco low-temperature oxide furnace at 300°C, providing a robust inorganic insulating layer (*26*).

An important aspect of designing microwire bundles for neural recording is controlling the wire-to-wire spacing. Insufficient spacing makes the bundle behave as a solid object during tissue insertion rather than a collection of individually penetrating microwires. Here, a sacrificial layer of parylene-C (PaC) was deposited via chemical vapor deposition (Labcoater) onto the glass-insulated wires to set the interwire spacing at two times the coating thickness (Fig. 2A, ii). Other materials could be used as well, but PaC was chosen for its chemical inertness, biocompatibility, and vapor-phase deposition (*27*). Figure 2 (B and C) shows a cross section from a bundle of 1000 wires 15 µm in diameter with 45-µm thick PaC, giving a center-to-center wire spacing of 100 µm. This distance could be varied from ≤1 to ≥150 µm depending on the desired spacing by altering the thickness of the PaC.

Mechanically bundling the wires was then performed either by a thread spooling tool (Optima 1100, Synthesis) commonly used in the textile industry or by cutting a spool of wire and manually collecting the wires together. The wires were inserted into a biomedical grade shrink wrap, which compressed the wires together into a honeycomb array, which was infiltrated with a biomedical epoxy (Epoxy

Technology Inc.) to create a consolidated structure (Fig. 2A, v). Bundles were then polished, and the proximal end was etched to expose 10 to 20 μm of the conductive wire for connection to the chip (Fig. 2D). Bundle size could be readily tuned for different applications: from a few hundred wires for mice, where the total size is constrained by the animal model, to >100,000 for high-bandwidth applications in larger mammals. Figure 1B emphasizes the scalability of this technique, showing a bundle of 8640 gold (Au) microwires with 10 μm of glass insulation, spaced at a 40-μm pitch.

After bundling, the microwires were released at the distal end by etching back the PaC coating and biomedical epoxy with oxygen plasma, exposing the wires for tissue insertion. Figure 2E shows the amount of volume displaced as a function of the wire-to-wire spacing. For 15-μm wires spaced at 100 μm, the size and density we used for in vivo recordings, assuming perfect packing (*28*), the volume displaced is 2%. Figure 2 (F to H) shows images of arrays of released wires, displaying uniform diameter and separation. The free length of the wires was controlled by the etching time and was varied from 0.5 mm to well over 1 cm depending on the tissue insertion depth desired. The maximum free length was limited by the material properties and buckling force threshold of the microwires. For example, 18-μm-diameter tungsten wires with lengths of >5 mm are feasible, while for 20-μm gold wires, lengths greater than 3 mm are likely to buckle upon insertion (*29*).

Different tip shapes are also possible through polishing or etching the ends of the wires (fig. S3, E to G). This was performed by bundling the wires together with a sacrificial polymer and polishing the bundle at an angle (<15° to 30°) on a lapping wheel. The angle-polished wires were then released and bundled together again with the desired spatial distribution. Alternatively, the wires could be individually electrosharpened (*30*) to form a <100-nm radius tip and then bundled together afterward. Studies measuring the force of microwire insertion into brain tissue have found microwire size and tip geometry to play an important role in the amount of brain dimpling during insertion (*29*).

If desired, the distribution of the individual microwire heights can be shaped into three-dimensional structures before the microwires are released from PaC and epoxy. Figure 2 (G and H) shows optical images of bundles with variable length wires. These can be produced in arbitrary shapes, for example, to simultaneously access cortical and subcortical regions. The shape is created by machining the epoxy-bonded bundle with a micromill (Minitech-GX MicroMill) or another tool into the desired shape.

Microwire bundle to CMOS interface

A key aspect of the design is developing a high-quality microwire-to-CMOS contact. This is a nontrivial problem, as either nonplanarities of the two surfaces or slight angular misalignment results in poor connectivity. The system must also be mechanically robust for long-term operation. Here, we overcame these challenges by revealing part of the bare metal microwire at the proximal end of the bundle (Fig. 3, A and B) and then mechanically compressing against the CMOS chip (Fig. 3B and fig. S3). Upon compression, the wires bent over (Fig. 3B) and "crimped" against the surface of the chip. Upon release, an imprint of the pixel can be seen on the wire core (Fig. 3B, top right inset, and fig. S3C). The height of the wires overcame nonplanar structures on the CMOS and subtle surface height variations, while the mechanical crimping provided a robust mechanical attachment.

After assembly of the microwire bundles, the organic and glass insulation of the microwires were etched back, revealing ~20 μm of bare metal microwire at the proximal end of the bundle (Fig. 3B). The free length could be chosen to be either less than the pixel-to-pixel spacing to avoid contacting adjacent pixels or longer to afford multiple pixel measurements of the same wire. To mechanically press the bundle and CMOS together, the bundle was fixtured with a threaded collet (Fig. 1D) and mounted into a passive, self-aligning mechanical press system designed around a flexible spring diaphragm (Fig. 3A and fig. S1) (*31*). This structure allowed the bundle to move vertically and tilt during contact, but not rotate or slide, allowing self-aligned contact but preventing scratching or abrasion of the surfaces.

The bundle was then gradually lowered into contact with the CMOS array by turning a threaded screw to extend the bundle (fig. S1, A, B, and E). Upon compression to the pixel array, each wire crimped, plastically deforming (Fig. 3B and fig. S3). This established reliable ohmic contact with the interfacing pixel and was highly uniform over the entire chip surface (Fig. 3), with all the wires tilting over in the same orientation (fig. S3D). The degree to which the wires plastically deform depended on the material; large deformations were observed with Au and little observed for W, yet both systems gave equivalent connectivity rates (>95%). After mechanical bonding, epoxy resin could be infiltrated to hold the bundle and chip together (Fig. 1D), although the mechanical press alone was sufficient to ensure no change in connectivity over 2 weeks. Furthermore, the interface was robust to mechanical impacts, such as flicking the bundle with a finger.

This process was highly flexible and agnostic to the identity of the chip; we successfully created bundle-to-chip interfaces with the imaging array chip from a Xenics Cheetah camera (327k pixels, 10 μm × 10 μm pixel with 20-μm pitch), an organic light-emitting diode (OLED) display chip from Olightek (1.44M pixels, 4 μm × 13 μm pixels), and a multielectrode array (MEA) device (25.6k pixels, 17 μm × 17 μm pixels) (*32*). The sizes and topologies of each of the pixels in these chips were different, ranging from polished flat Au surfaces to windowed pixels with Al contacts (fig. S3A). If desired, Pt contact pads could be lithographically deposited onto the surface of the pixels to increase the electrically active contact area (fig. S3B).

After mating, the microwire-to-pixel connectivity yield was measured by the electrical conductivity and noise characteristics of each pixel. Connectivity between the bundle and chip was high, with >90% of the wires contacting a pixel reproducibly. Figure S2G shows a connectivity map of a bundle of 184 wires, with 177 successfully contacted (96% yield). Highlighting the scalability of this process, Fig. 3D shows the connectivity of the central region of the 8640-wire bundle (~7-mm diameter, 40-μm pitch, 18-μm-diameter microwires; Figs. 1D and 3C) mated to an MEA chip (Xenics Cheetah camera) with >90% of the wires connected to an active pixel (Fig. 3, C and D).

While the microwires are inherently laid out in a hexagonal fashion, the pixels are in a square or rectangular array, which intrinsically presents an alignment challenge. In practice, there are generally many more pixels available than wires, and the need for 1:1 alignment is not an issue. One possible scenario is a single microwire contacts two or more pixels, which provides additional measurements of the same wire. The other scenario, having more than one microwire contacting a single pixel, should be avoided as separation of the two signals is problematic. This situation can be avoided as long as the distance between wires (l_{wire}) is greater than $l_{pixel}\sqrt{2}$, where l_{pixel} is the width of the pixels' active area. As an example, the anticipated

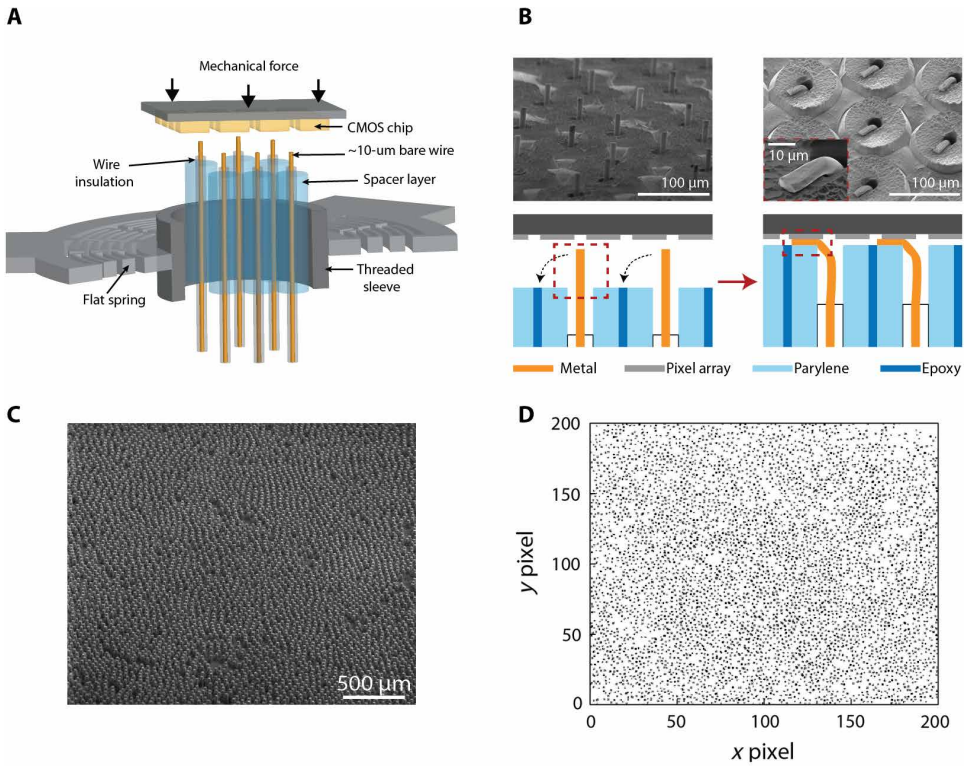

Fig. 3. Microwire bonding to CMOS. (**A**) Design schematic. The microwires are held by a flat anisotropic spring with a threaded sleeve and mechanically lowered onto the CMOS chip until high connectivity is achieved. (**B**) Before bonding, the insulation of the distal end is etched back, leaving ~10 to 20 μm of bare metal wire. After mechanically pressing to the CMOS chip, these bare wires are mechanically crimped, allowing good electrical contact even with nonplanar pixel surfaces. (**C**) SEM focusing on ~4500 wires of the 8640 bundle shown in Fig. 1B with the corresponding connectivity map. (**D**) Each black pixel from the IR camera chip shows a pixel electrically connected to a wire. More than 90% wire-to-pixel connectivity was achieved.

connectivity as a function of pixel pitch was calculated from the average number of contacts over all possible lateral and rotation orientations (Fig. 4A). We assumed a metal microwire diameter of 15 μm and a pixel pitch of 17 μm with a metallic contact area 50% of the per-pixel area (fill factor), similar to the experimental conditions. Figure 4 (A and B) shows that 100% of the wires will always contact one or more pixels, and with microwire spacing >18 μm, no pixel will contact more than one wire. This corresponds well with the actual experimental measurements, which found >90% connectivity yields even with no effort to align pixels to wires. Examples of multiple wires contacting a single pixel only occurred for large pixels, with pitches greater than the wire-to-wire pitch. Given that modern camera imagers have pixels ~1 to 10 μm on a side and displays on the order of 10 to 20 μm on a side, alignment of the bundles and CMOS is not necessary given our wire pitches (order of 25 to 100 μm). One possible issue is that the metallic contact pads may be recessed or much smaller than the overall pixel footprint. In this case, the pixels can be lithographically modified to enlarge the metallic contact region, such as shown in the inset of Fig. 4D.

Electrical performance and in situ electrodeposition through CMOS

The electrical characteristics of the microwires were assessed to determine whether the mating process increased the recording noise in the CMOS sensor array. First, the impedance properties of individual wires of four different metals (Au, PtW 92/8, PtIr 90/10, and W) were characterized between 0.1 and 1 MHz in phosphate-buffered saline (PBS). Tests of individual wires found impedances of <1 megohm at 1 kHz and were strongly dependent on wire material and diameter. This could be substantially reduced by electrodeposition of impedance-lowering materials such as iridium oxide (IrOx) or poly(3,4-ethylenedioxythiophene) polystyrene sulfonate (PEDOT:PSS) on the tip of the electrodes (*18*). This could be done either by electrically connecting all the wires together and depositing on the array in parallel or by taking advantage of the wires' connection to the CMOS to electrochemically deposit on each wire individually. We used a commercial OLED display chip from Olightek to electrochemically deposit IrOx on each wire in a bundle individually, showing a substantial reduction in impedance (Fig. 4C). The use of the CMOS chip provides a unique method to electrochemically deposit low-impedance materials (IrOx, PEDOT:PSS) on an array of hundreds to thousands of wires simultaneously with control to improve the quality of neural recordings. While all materials tested were capable of recording single units during acute recordings, PtIr 90/10 was chosen as the preferred material because of its low impedance (200 ± 27 kilohms) and long-term biocompatibility (*33*).

One possible concern with bonding an array of metal wires to a CMOS device is increased noise. We tested the electrical pixel noise before and after bundle mating to a multielectrode CMOS chip previously demonstrated for in vitro measurements (*32*). The chip has 26,400 pixels, 1024 of which can be addressed simultaneously at 20 kHz with stimulation from 32 independent sites, and is commercially

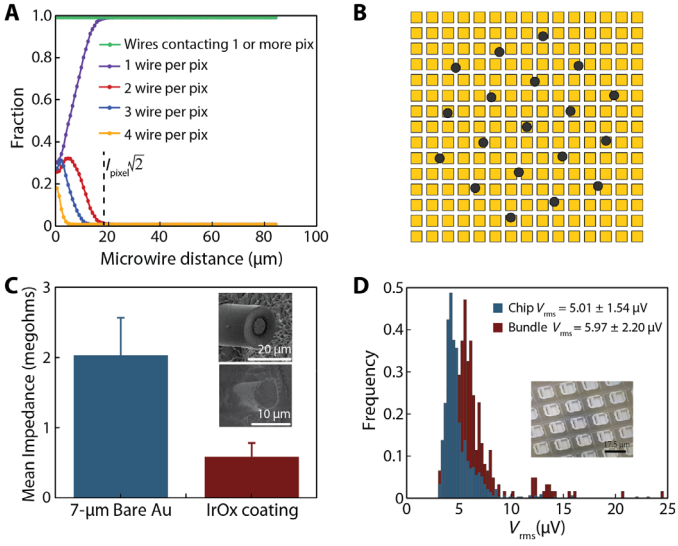

Fig. 4. Noise characteristics and wire connectivity. (**A**) A hexagonal array of microwires 15 μm in diameter can easily achieve 100% connectivity to one or more pixels (green trace) without alignment. Further, no pixels will have more than one wire attached if the wire spacing is greater than $l_{pixel}\sqrt{2}$, where l_{pixel} is the width of the pixels' active area. (**B**) Schematic of the hexagonally arranged microwires overlaid on a square pixel array, showing that alignment is not necessary to achieve unity connectivity yields when the number of pixels is much greater than the number of wires. (**C**) Average impedance values of a bundle of 150 Au microwires before (inset 1) and after in situ electrodeposition (inset 2), measured at 1 kHz. An OLED display chip was used to apply a voltage to individual wires to electrochemically deposit IrOx. (**D**) RMS noise of the bare high-resolution CMOS MEA chip (blue), and the same chip after bonding a microwire bundle of 251 PtIr wires, 15 μm in diameter (red). The noise increased from 5.0 ± 1.5 μV (10 Hz to 10 kHz) for the bare chip to 6.0 ± 2.2 μV after addition of the bundle, showing that the bundle and the mating process did not introduce substantial noise. (D) Inset: Scanning electron micrograph (SEM) of Pt deposition on the CMOS array to improve electrical contact.

available (Maxwell Biosystems Inc.). The recording noise on the unmodified pixels is low, 5.0 ± 1.5 μV root mean square (RMS) (10 to 10 kHz), enabling robust electrophysiological recordings and stimulation. Pt pads were lithographically added to increase the pixel contact area to 50% of the pixel (Fig. 3D, inset), providing robust heterogeneous integration (>95% connectivity) for all bundles. After mechanical pressing, the noise was measured on each channel of a bundle of 251 microwires of 15-μm-diameter PtIr cores with 1-μm glass insulation, spaced at 100 μm apart (Fig. 4D). The RMS noise after bundle contact was ≤5.97 ± 2.2 μV RMS, minimally higher than the unconnected chip itself (both noise figures were measured in saline and include the electrode-solution interface contribution) and well within the tolerable range for in vivo recordings.

To assess the temporal stability of the microwire bundle–CMOS interface, the bundle was left pressed for 14 days, and a noise measurement was performed every day (fig. S2, I and J). No differences were observed in the connectivity and minor fluctuations in the average noise over this period. Collectively, these measurements show that the addition of the bundle to the CMOS added very little noise to the system, even for relatively long electrodes (7.5 cm), and is mechanically and temporally robust. Figure S2 shows the noise characterization for several different microwire bundle materials and configurations, all demonstrating minimal additional noise relative to the bare chip.

Retinal recordings

To test the ability of the completed device to record neural activity across a planar surface, we used an ex vivo preparation of rat retina, where previous efforts at large-scale electrical recordings from retinal ganglion cells (RGCs) provide a performance baseline (*34*–*36*). A dialysis membrane held a small piece of isolated retina against the bundle in a perfusion chamber (Fig. 5A), and then a 138-wire bundle [mated to the high-resolution CMOS MEA (*32*)] was lowered into contact with the retina. Activity was recorded in response to both steady, ambient light and a pulsed visual stimulus, and spikes were sorted using standard procedures [Mountainsort (*37*), see Materials and Methods]. Recorded spikes presented typical single-unit signatures, i.e., a localized detected action potential at one wire with smaller peaks on adjacent wires (Fig. 5A). The highlighted spike waveform in each box is a single unit, and the traces around it are the electrical activity on nearby channels at the times that unit fired. Spiking activity was recorded with high yield (total 152 units; 1.1 units per wire) and high signal-to-noise ratio (>4.5× SD) (Fig. 5B, filtered voltage traces). Increases in spiking activity were observed during the light stimulation pulse, particularly at its onset and offset (Fig. 5, C and D). This corresponds to the known existence of ON- and OFF-type RGCs that respond transiently to light steps, evidence that the spikes were RGC activity. These retinal recordings demonstrate the ability of the system to record single units at high data acquisition rates and high signal-to-noise.

In vivo recording in awake moving mice

Next, we tested whether it was possible to record neural activity in deep cortical and subcortical areas across a large spatial region in rodents in vivo. The total number of electrodes in the bundle was constrained by the size of animal model. To accommodate the mouse brain, bundles were fabricated to total diameters ranging from 1.75 to 3.5 mm, thus containing 135 to 251 PtIr microwires (15-μm PtIr core, 1-μm glass coating, and length 1 to 2 mm). This number of electrodes was chosen to maintain ~100-μm separation between individual wires, allowing straightforward insertion and minimizing tissue damage. Larger arrays may be feasible for larger animals.

The bundles were flat-polished with ~100-μm spacing between wires to minimally perturb the brain and reduce the likelihood of trauma to the brain and reduced neural activity (*38*). Under these conditions, the microwire bundle displaces at most ~2% of the tissue volume during insertion (Fig. 2E). To confirm insertion, we coated the microwires with DiI (1.5 mg/ml) and performed post hoc confocal imaging (fig. S4).

Recordings were performed acutely within 2 hours of bundle implantation in deep layers of motor and somatosensory cortices and the dorsal striatum. Mice were allowed to run voluntarily on a spherical treadmill, floated with air pressure, in a head-constrained condition while recording with the bundle and high-resolution CMOS-MEA interface (*32*) (Fig. 6A) (*39*). Spiking activity was readily observed in most of the wires in the bundles across a horizontal layer (Fig. 6B). Around 100 to more than 200 putative neurons (92 to 221 neurons, see Materials and Methods) were reliably identified across a large horizontally extended area in each recording during a typical 5-min recording session, which yielded 0.56 ± 0.11 (0.3 to 0.89) single units per wire.

In recordings from motor cortex, spiking activity was highly correlated with motion (Fig. 6, C and D), consistent with previous findings (*40*–*43*). Significantly higher spiking rates were observed during

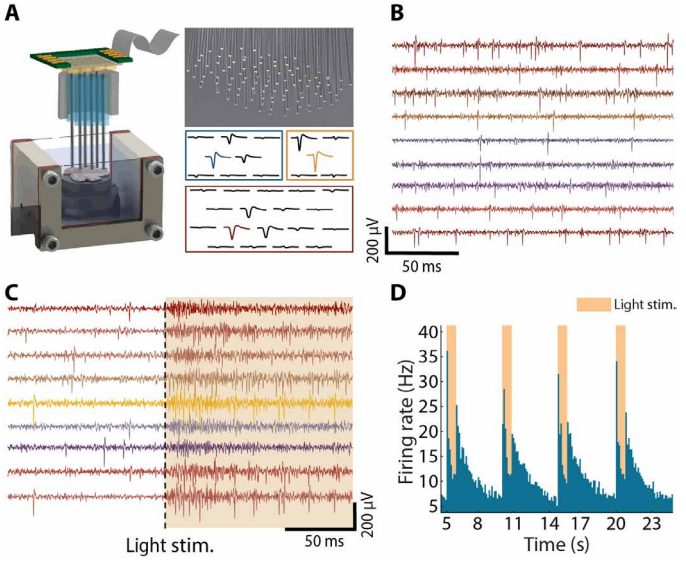

Fig. 5. Retinal recordings. (**A**) Custom-built perfusion chamber used for dissected retina recordings. The retina sits elevated on a dialysis membrane. Sample waveform distribution across a microwire bundle from retinal recordings. (**B**) Recordings of spontaneous firing of RGCs. (**C**) Firing of RGCs in response to light stimulation delivered at the time indicated by the dashed line. (**D**) A histogram of the average firing rate of all neurons detected, showing an increase immediately following and immediately after light stimulation.

continuous running sessions compared to the quiescent state (quiescent, 8.4 ± 1.8 spikes/s; running, 20.1 ± 2.1 spikes/s; $P < 0.001$, $n = 30$ trials, paired t test; Fig. 6, D and E). In a separate experiment, striatal neural activity was recorded with a bundle of microwires with 2 mm of free length to access subcortical regions (Fig. 6F). Spiking activity of striatal neurons was also correlated with the behavioral states (quiescent, 13.1 ± 1.7 spikes/s; running, 18.1 ± 2.0 spikes/s; $P < 0.01$, $n = 30$ trials, paired t test; Fig. 6E). In addition to neural spiking, the rhythmic fluctuations of cortical circuits exhibit strong state-dependent changes (*44*–*46*). We found that low-amplitude local field potential (LFP) fluctuations, especially in the gamma band (30 to 80 Hz), were significantly larger during free exploration and running states than in the quiescent state (relative gamma band power: quiescent, 0.049 ± 0.012; running, 0.141 ± 0.043; $P < 0.01$, $n = 30$ sessions; Fig. 6G), consistent with previous reports (*47*, *48*).

Compared to in vivo imaging techniques, commonly used for monitoring large populations (hundreds to thousands) of neural activity, CMOS-bundle devices have several benefits. Conventional two-photon imaging typically records neural activity limited to video frame rates, and temporal resolution is further sacrificed when recording from large brain areas (*49*). In addition, imaging techniques are usually limited by tissue scattering and can only be used to record superficial areas without removing brain tissue. For imaging subcortical and deep brain areas, a portion of the brain tissue is removed (*4*, *49*–*51*). In comparison, microwire bundles mated to CMOS arrays can record spiking activity from hundreds of neurons and LFPs simultaneously with large spatial extent, albeit with lower spatial resolution, while retaining the benefits of >10-kHz temporal resolution in electrophysiological recordings. In addition, the flexibility of fabricating the length of the distal end of the bundle with single wire precision enables dense recordings from subcortical areas, such as the striatum (Fig. 6F), without removing the cortical areas above.

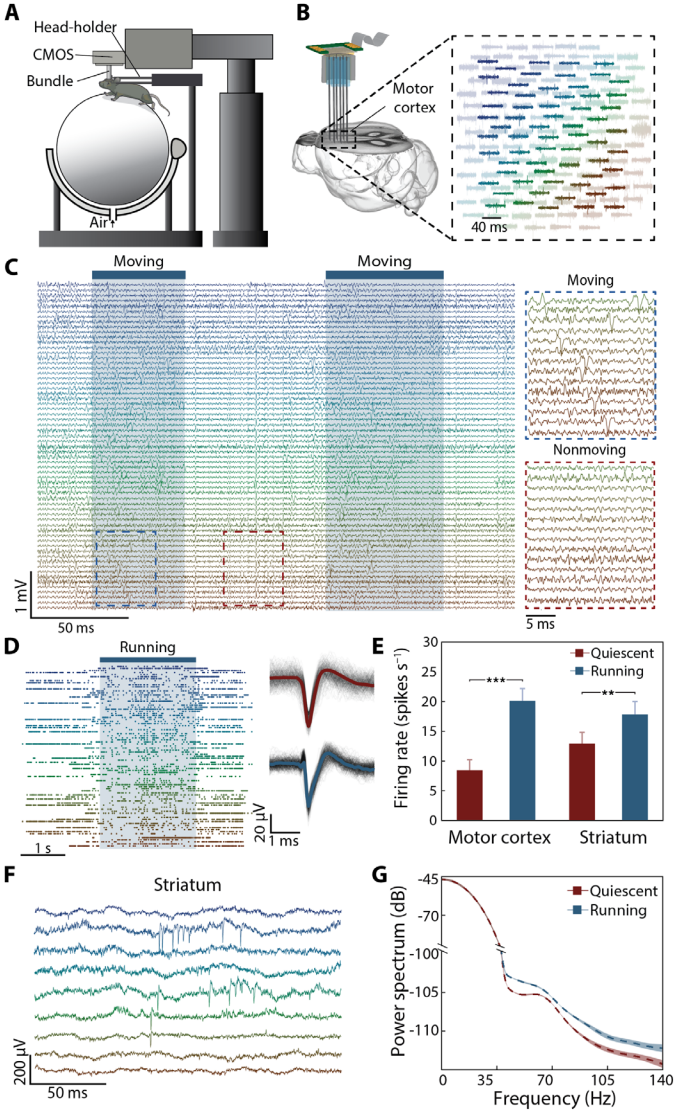

Fig. 6. In vivo recording in awake moving mice. (**A**) A schematic of the in vivo recording setup. (**B**) Left: Illustration of recording across a large spatial extent with a microwire bundle in the motor cortex. Right: Representative traces of electrophysiological activity (300 to 6000 Hz) from 163 microwires (background traces). Highlighted traces from 67 wires show neural action potentials of a 50-ms snapshot of motor cortical activity during motion. The color code represents the relative positions of the microwires. (**C**) Representative traces showing detailed motor cortical activity from the 67 wires highlighted in (B). The shaded areas indicate the moving episodes of the mouse. Insets show a close look of the representative traces during moving (top) and nonmoving (bottom) states. (**D**) Raster plot of detected units after spike sorting in a motor cortical recording. Insets show two representative spike-averaged waveforms. Gray traces are 400 randomly selected raw waveforms of two representative detected spikes. (**E**) Significantly higher spiking rates were observed during running in both motor cortical and striatal recordings (motor cortex: ***$P < 0.001$ and striatum: **$P < 0.01$; 30 trials in both areas). (**F**) Representative traces (unfiltered) of striatal recording. Both fluctuation in LFP and neural spikes were observed. (**G**) Gamma band power was significantly larger during running compared with the quiescent state in the striatum ($P < 0.01$; 30 trials).

Shaping the distal end of the bundle also enables simultaneous access to depths in multiple brain areas. The scalability of this approach is applicable for massive-scale bundle recordings in larger animals, which is particularly challenging for imaging approaches.

CONCLUSION

We have demonstrated an effective method to combine the rapid progress in CMOS devices together with brain tissue–compatible probes. Neural recording technologies are rapidly developing, yet are largely based on planar probes (e.g., Michigan Probes, Neuropixels, and Neuroseeker) or micromachined silicon arrays (Blackrock Utah arrays). This approach offers a third alternative, retaining the low tissue damage of small microwires, while enabling rapid application of cutting-edge silicon array technology to neuroscience. Additional advances in CMOS technology, such as low-artifact stimulation (*52*), higher channel counts (*53*), and electrochemical monitoring (*54*, *55*), can be rapidly deployed using this system. Our design is favorable for recording or stimulation experiments that require large area coverage and high density.

Improvements to minimize the geometrical device and connector form factors are underway, allowing the animal to freely move while recording and/or modulating electrophysiological activity. Subdural implantation may also be possible considering the low power consumption of the neural chip used (<70 mW) (*56*). Because of the control over the depth of each microwire, sampling deep lateral and vertical structures is possible simultaneously with chronic floating microwire-based brain-machine interfaces while maintaining ultralow volumetric perturbation of the tissue. The microwire interface provides the link between biological tissue and CMOS electronic technology, enabling the rapid development of silicon-based devices to brain-machine interfaces that can readily scale in channel count, temporal resolution, and sensitivity.

MATERIALS AND METHODS

Microwire bundles

To fabricate insulated microwires in-house, PtIr, W, and PtW microwires of varying diameters (5 to 125 μm) were purchased from Goodfellow Inc. Using a custom spooling rig, microwires were wrapped from their spool onto a custom rack wherein each wire was spaced by ~500 μm, allowing for subsequent chemical vapor deposition processing. Silica deposition was performed at 300°C in a low-pressure chemical vapor deposition furnace (Stanford Nanofabrication Facility). A custom rack allowed for >1 km of microwire to be coated at the same time. Using the same rack, PaC was deposited using chemical vapor deposition (SCS Labcoater 2) to desired thickness, determining the interwire separation. Wires were subsequently cut and mechanically bundled together, naturally aggregating into a honeycomb hexagonal array, via shrink wrap. Bundles were then embedded in a biomedical grade epoxy (EpoTek 301, Epoxy Technology Inc.) and cured at 65°C for 2 hours. Bundles were then placed into borosilicate glass tubes (6-mm outer diameter and 4-mm inner diameter) to aid in handling and sealed using the same epoxy. Polishing of both ends of the bundle was carried out by successive SiC-based grit (Buehler, CarbiMet S, 600, 1000, and 1200), terminating in a hardened silica slurry on a polyester mesh, accomplishing <10-nm RMS roughness. The bundle ends were then washed with soap, distilled water, and isopropyl alcohol.

After polishing, one end of the bundle (proximal end) was dipped in Crystalbond (SPI Crystalbond 509) to protect the polished surface. The distal side, the "neuronal end", underwent a piranha etch (three parts concentrated sulfuric acid and one part 30% hydrogen peroxide) for 5 min to remove the epoxy embedded between the wires and subsequently washed with soap and distilled water. The bundle was placed in an oxygen plasma to etch away PaC on the "tissue end," exposing the glass-ensheathed microwires. The free length of the microwire was determined by the depth of the piranha etch, as the epoxy between the parylene-coated wires substantially reduces the etch rate (lateral versus vertical etching). After plasma etching, the wires were cleaned with soap and distilled water. To prepare the proximal end, the Crystalbond was removed by placing the bundle in acetone and placed back in the oxygen plasma briefly to etch ~1 to 20 μm of epoxy and parylene between the microwires. The proximal end was then submerged in a 2% hydrofluoric acid etch for 8 min to remove the glass coating on the microwires.

To alter tip geometry and/or add a Pt-black coating to lower electrode-electrolyte impedance, microwires coated with glass and PaC were placed into a glass tube and infiltrated with Apeizon black wax W. Polishing of the wire aggregate occurred at the desired angle, typically performed at 24° to produce an acute tip shape. Sputtering of Pt with a high Ar flow rate produced the Pt black tip coatings. Coated microwires were released in toluene, dissolving the binding agent. Subsequent bonding is carried out as described previously. An alternative process was the use of micromachining the distal end, terminating with the use of a grit-based tooling bit to polish the machined surface (Fig. 2, G and H). The distal end of this bundle was then etched with oxygen plasma to release the individual wires. The glass layer is unaffected by the oxygen plasma, still providing electrical insulation. The proximal end was processed as described previously.

Impedance measurements

The impedance properties of individual wires of five different metals (Au, Pt, PtIr 90/10, W, and Pt black–coated W) were characterized between 0.1 and 1 MHz in 150 mM PBS with a Ag/AgCl reference electrode (Gamry Instruments Reference 600+). Tests of individual wires found impedances of <1 megohm at 1 kHz and were strongly dependent on wire material and diameter.

Passive mechanical press system and microwire bundle to CMOS interface

To align two flat surfaces (bundle of microwires and pixel array) such that they are perfectly parallel, ensuring a reliable press, we developed a passive (no active electric components), self-aligning press system. The design is structured around a parasitic error-free symmetric diaphragm flexure seen in fig. S1. The flexible diaphragm (FD) was designed to restrict motion along the x and y axes and rotation about the z axis (yaw; parasitic twist), while allowing for motion about the z axis and rotation about the x and y axes (row and pitch, respectively). This allows two flat surfaces to come into even contact when pressed, while maintaining pressure on the two surfaces as proportional to the FD's spring constant. The design of the FD was adopted from Awtar *et al.* (*31*), exploiting symmetry to eliminate parasitic twist associated with traditional FD designs when deflected. We show the design of our FD, constructed from spring steel and fabricated via photochemical machining (PCM) (fig. S1C). In this design, 16 peripheral flexure arms are used, despite only four being needed to create a symmetrical design. This was done to reduce variation in angular stiffness with in-plane axes passing through the diaphragm center. The hollow center of the diaphragm allows for placement of the microwire bundle (fig. S1B). The spring constant of the FD was defined lithographically by the width of the flexure arms and the thickness of the spring steel used. To minimize material creep, small

deflections of the FD were maintained, as it was desirable for some experimental settings to keep the microwire bundle pressed for weeks at a time. The design of the FD also has three emanating appendices used to grip the FD and restrict its motion in rotating about the *x* and *y* axes when being pressed into contact. To accurately control the press, a threaded design with a nut was used, allowing the user to slowly screw down the FD and contained microwire bundle until the diaphragm was visibly deflected or high connectivity was observed. Three tightly specified machined slots were placed onto the male threaded component, allowing for placement of the three emanating appendices of the FD. This prevented rotation of the FD and contained microwire bundle, while still allowing for the screwing mechanism to press the bundle onto the pixel array. To account for the backlash between the male and female threading, an external wave spring was added to constantly keep pressure off of the FD and male threaded nut (fig. S1E). In this way, by screwing the nut, vertical displacement of the FD and contained microwire bundle can be controlled. Consequently, the force observed by the chip was dictated by the amount of displacement allotted by the vertical displacement of the FD according to Hooke's law.

The FDs are made via PCM, out of spring steel (0.007 inches thick). Flexure arm width and spring steel thickness are varied to alter the spring constant of the diaphragm along the perpendicular *z* axis. The mechanical press body was machined out of Al and anodized. The nut was made of brass to prevent material catching. The external wave spring was custom-made to fit the geometry of the press system. A collet was machined and glued to the bundle via cyanoacrylate. The FD rested on the end of the collet and was compressed via a corresponding female nut. To bring the microwire bundle into contact with the pixel array, the external nut was rotated, until the flexure arms of the FD were deflected (fig. S1E). The protruding metallic wires on the proximal end are compressed onto the pixel array using the passive mechanical press system, crimping to establish ohmic contact.

CMOS lithographic modifications

Both the infrared (IR) read-out integrated circuit (ROIC) (*57*) and the high-resolution CMOS MEA (*32*) had recessed contact pads. In the case of the latter, alternating SiO_2 and SiN layers were placed to passivate for high-resolution CMOS MEA use. To lithographically pattern the surface of the CMOS, Microposit SPR 220-7 was spun into the surface. Exposure of the desired pixels was done using a maskless aligner (Heidelberg Instruments Inc.). Following development, sputtering of a 5/300/5/30-nm stack Ti/Al/Ti/Pt followed as Al can be deposited thick without issues of film stress. Lift-off in acetone was done to complete the lithographic modifications. Chips were then wire-bonded to the custom PCBs.

High-resolution CMOS MEA

The high-resolution CMOS MEA was operated as described by previous work (*32*). After pressing the microwire bundles onto the CMOS MEA, the distal end of the bundle was submerged in 150 mM PBS with a reference electrode of corresponding metallic core material (Pt or W). We applied a 1-kHz, 1-mV sinusoidal waveform at the reference voltage of the CMOS MEA (1.65 V) and scanned through the 26,400 electrodes using an SRS DS360 wave function generator. The electrodes with a wire connected would record the sine waveform, and the pixel position was noted to determine which electrodes to route the channels to (connectivity map). After establishing the connectivity map, noise was measured by placing the reference electrode (Pt) into the saline bath.

IR camera chip

Initial characterization of heterogeneous integration was performed with a modified Cheetah 640 CL IR camera (20-μm pitch, 640 × 512 array; Xenics, Leuven). Upon request, the photosensitive layer was omitted by the manufacturer. In place of standard indium bump pads, lithographic modifications were performed on the top layer of the ROIC, elevating the electrode pads to optimize for heterogeneous integration of microwire electrode bundle to chip array. Sampling frequency is correlated with sampling size, ranging from 1.7 to 200 kHz (largest sampling size to smallest). For the 8640-microwire bundle shown in Fig. 1B, recordings were carried out at 32 kHz. Each pixel of the Cheetah 640 ROIC contains a transimpedance amplifier with a feedback capacitor of 7fF. Voltage signals in the brain result in current flow and charge accumulation across the feedback capacitor. For calibration, an SRS DS360 wave function generator was used to apply the input signal. Noise measurements and gain measurements were performed as described in the earlier section.

Animals

Adult (4 to 6 months) C57BL/6J mice (JAX no. 000664) and wild-type Long-Evans rats were used for this study. All procedures were approved by Stanford University's Administrative Panel on Laboratory Animal Care.

Ex vivo rat retinal recordings

Eyes were enucleated after decapitation of deeply anesthetized wild-type Long-Evans rats, in accordance with institutional guidelines for the care and use of animals. Immediately after enucleation, the anterior portion of the eye and vitreous were removed in room light, and the eye cup was placed in a bicarbonate-buffered Ames' solution (Sigma-Aldrich, St. Louis, MO). Under infrared illumination, pieces of retina 3 to 5 mm in diameter were isolated from the sclera and placed ganglion cell side up on dialysis membrane in the perfusion chamber. The microwire bundle was lowered into the chamber until it made contact with the retina, holding it in place against the membrane. The preparation was perfused with Ames' solution bubbled with 95% O_2 and 5% CO_2 and maintained at roughly 30°C and pH 7.4 using an in-line heater. Spontaneous recordings were performed under low, ambient light, and pulsed stimulation consisted of a white, full-field pulse delivered with a handheld flashlight lasting roughly 1 s, followed by roughly 4 s of darkness. The recorded data were filtered (band pass, 300 to 6000 Hz), and spike sorting was performed using Mountainsort as discussed in the "Data processing and analysis" section.

Mouse surgery and in vivo recordings

Mice were anesthetized with isoflurane and positioned in a stereotaxic frame. Three skull screws were implanted to provide mechanical stability and for use as ground and reference electrodes. Head plates made of titanium were centered to the intended recording site on the right hemisphere and fixed to the screws and skull with C&B Metabond cement (Parkell). A 3- to 5-mm craniotomy was made over the recording sites (motor cortex: 1 mm Anterior-Posterior (AP), 2 mm Medial-Lateral (ML), and 1.8 mm Dorsal-Ventral (DV); somatosensory cortex: −1.5 mm AP, 2.5 mm ML, and 1 mm DV; dorsal striatum: 1 mm AP, 2 mm ML, and 3 mm DV). Dura was

carefully removed to facilitate bundle insertion (fig. S4A). The mouse was then transferred to the experimental apparatus and allowed to recover from anesthesia. The head mount was positioned on top of a floating Styrofoam ball to allow for movement as described in Bennett *et al.* (*39*). The bundle was inserted through the craniotomy manually, piercing the pia mater. After slow insertion to the final depth, electrophysiological activity was acquired within 2 hours.

The high-resolution CMOS MEA operates at a floating voltage of 1.65 V. Consequently, the animal was isolated from ground (electrically "floating") by connecting the reference of the chip to the skull screws. The bundles used in Fig. 6 (B to D) and Fig. 6F consisted of 138 and 251 microwires, respectively, of 15-μm-diameter PtIr core with 1-μm SiO_2 insulative cladding and 100-μm pitch. Motion classification was verified by simultaneously recorded behavior data, in which the running and quiescent periods corresponded well to the active and nonactive states of our classification criterion, respectively.

Data processing and analysis

Data analysis was performed using custom software written in Python 3.6.3 (Anaconda linux-64 v7.2.0 distribution, Anaconda Inc.) and MATLAB 2018a (Mathworks). Clustering was performed using Mountainsort (*37*), with an event detection threshold set to 4.5 SD. Putative single units were identified using noise overlap and isolation thresholds described by Chung *et al.* (*37*) (noise overlap < 0.03; isolation > 0.95) and further confirmed by manual curation. The putative single units typically had a negative peak at the recording site, with smaller negative peaks at adjacent sites. Each putative single unit was recorded on ~1.4 sites, which is in agreement with the spacing between the electrode sites (*58*). No effort was made to further tailor clustering and unit identification to the recording configuration, which could further increase unit yield.

Ultrashort-duration (<0.5 ms), "triphasic", symmetric waveforms, consistent with axonal spikes (*59*), could also be identified with amplitudes of ~20 to 40 μV, with ~4.5 times signal-to-noise ratio. Signals with positive polarity occasionally occur at the same time as large negative spikes on nearby electrodes, but the delay between positive peaks with respect to the dominant negative peak on nearby channels varies between recording sites. This behavior is carefully studied by Bakkum *et al.* in acute mouse cerebellar slices and rat cortical cultures, possibly representing dendritic activity, but further work is needed to substantiate whether this is the same phenomena we observe in vivo (*9*, *60*).

SUPPLEMENTARY MATERIALS

Supplementary material for this article is available at http://advances.sciencemag.org/cgi/content/full/6/12/eaay2789/DC1

Fig. S1. Passive mechanical press system.

Fig. S2. Connectivity maps and RMS noise distribution from bundles made with different materials.

Fig. S3. Chip and bundle modifications.

Fig. S4. Confirmation of acute insertion of microwire bundle.

Fig. S5. Histology.

View/request a protocol for this paper from *Bio-protocol*.

REFERENCES AND NOTES

1. O. Gschwend, J. Beroud, R. Vincis, I. Rodriguez, A. Carleton, Dense encoding of natural odorants by ensembles of sparsely activated neurons in the olfactory bulb. *Sci. Rep.* **6**, 36514 (2016).
2. K. Miura, Z. F. Mainen, N. Uchida, Odor representations in olfactory cortex: Distributed rate coding and decorrelated population activity. *Neuron* **74**, 1087–1098 (2012).
3. S. D. Antic, R. M. Empson, T. Knöpfel, Voltage imaging to understand connections and functions of neuronal circuits. *J. Neurophysiol.* **116**, 135–152 (2016).
4. D. A. Dombeck, C. D. Harvey, L. Tian, L. L. Looger, D. W. Tank, Functional imaging of hippocampal place cells at cellular resolution during virtual navigation. *Nat. Neurosci.* **13**, 1433–1440 (2010).
5. M. N. Economo, N. G. Clack, L. D. Lavis, C. R. Gerfen, K. Svoboda, E. W. Myers, J. Chandrashekar, A platform for brain-wide imaging and reconstruction of individual neurons. *ELife* **5**, (2016).
6. G. Buzsáki, A. Draughn, Neuronal oscillations in cortical networks. *Science* **304**, 1926–1929 (2004).
7. A. Mizrahi, J. C. Crowley, E. Shtoyerman, L. C. Katz, High-resolution in vivo imaging of hippocampal dendrites and spines. *J. Neurosci.* **24**, 3147–3151 (2004).
8. Y. Ziv, L. D. Burns, E. D. Cocker, E. O. Hamel, K. K. Ghosh, L. J. Kitch, A. El Gamal, M. J. Schnitzer, Long-term dynamics of CA1 hippocampal place codes. *Nat. Neurosci.* **16**, 264–266 (2013).
9. D. Khodagholy, J. N. Gelinas, T. Thesen, W. Doyle, O. Devinsky, G. G. Malliaras, G. Buzsáki, NeuroGrid: Recording action potentials from the surface of the brain. *Nat. Neurosci.* **18**, 310–315 (2015).
10. J. J. Jun, N. A. Steinmetz, J. H. Siegle, D. J. Denman, M. Bauza, B. Barbarits, A. K. Lee, C. A. Anastassiou, A. Andrei, Ç. Aydin, M. Barbic, T. J. Blanche, V. Bonin, J. Couto, B. Dutta, S. L. Gratiy, D. A. Gutnisky, M. Häusser, B. Karsh, P. Ledochowitsch, C. M. Lopez, C. Mitelut, S. Musa, M. Okun, M. Pachitariu, J. Putzeys, P. D. Rich, C. Rossant, W.-L. Sun, K. Svoboda, M. Carandini, K. D. Harris, C. Koch, J. O'Keefe, T. D. Harris, Fully integrated silicon probes for high-density recording of neural activity. *Nature* **551**, 232–236 (2017).
11. M. B. Ahrens, M. B. Orger, D. N. Robson, J. M. Li, P. J. Keller, Whole-brain functional imaging at cellular resolution using light-sheet microscopy. *Nat. Methods* **10**, 413–420 (2013).
12. C. T. Nordhausen, E. M. Maynard, R. A. Normann, Single unit recording capabilities of a 100 microelectrode array. *Brain Res.* **726**, 129–140 (1996).
13. A. Maccione, M. Garofalo, T. Nieus, M. Tedesco, L. Berdondini, S. Martinoia, Multiscale functional connectivity estimation on low-density neuronal cultures recorded by high-density CMOS micro electrode arrays. *J. Neurosci. Methods* **207**, 161–171 (2012).
14. J. Müller, M. Ballini, P. Livi, Y. H. Chen, M. Radivojevic, A. Shadmani, V. Viswam, I. L. Jones, M. Fiscella, R. Diggelmann, A. Stettler, U. Frey, D. J. Bakkum, A. Hierlemann, High-resolution CMOS MEA platform to study neurons at subcellular, cellular, and network levels. *Lab Chip* **15**, 2767–2780 (2015).
15. D. Scribner, L. Johnson, P. Skeath, R. Klein, D. Ilg, L. Wasserman, N. Fernandez, W. Freeman, J. Peele, F. K. Perkins, E. J. Friebele, W. E. Bassett, J. G. Howard, W. Krebs, A retinal prosthesis technology based on CMOS microelectronics and microwire glass electrodes. *IEEE Trans. Biomed. Circuits Syst.* **1**, 73–84 (2007).
16. I. H. Stevenson, K. P. Kording, How advances in neural recording affect data analysis. *Nat. Neurosci.* **14**, 139–142 (2011).
17. A. H. Marblestone, B. M. Zamft, Y. G. Maguire, M. G. Shapiro, T. R. Cybulski, J. I. Glaser, D. Amodei, P. B. Stranges, R. Kalhor, D. A. Dalrymple, D. Seo, E. Alon, M. M. Maharbiz, J. M. Carmena, J. M. Rabaey, E. S. Boyden, G. M. Church, K. P. Kording, Physical principles for scalable neural recording. *Front. Comput. Neurosci.* **7**, 137 (2013).
18. M. Kollo, R. Racz, M. Hanna, A. Obaid, M. R. Angle, W. Wray, Y. Kong, A. Hierlemann, J. Müller, N. A. Melosh, A. T. Schaefer, CHIME: CMOS-hosted in-vivo microelectrodes for massively scalable neuronal recordings. *bioRxiv*, 570069 (2019).
19. Z. J. Du, C. L. Kolarcik, T. D. Y. Kozai, S. D. Luebben, S. A. Sapp, X. S. Zheng, J. A. Nabity, X. T. Cui, Ultrasoft microwire neural electrodes improve chronic tissue integration. *Acta Biomater.* **53**, 46–58 (2017).
20. M. A. L. Nicolelis, Ed. *Methods for Neural Ensemble Recordings* (CRC Press/Taylor & Francis, ed. 2, 2008).
21. J. C. Williams, R. L. Rennaker, D. R. Kipke, Long-term neural recording characteristics of wire microelectrode arrays implanted in cerebral cortex. *Brain Res. Brain Res. Protoc.* **4**, 303–313 (1999).
22. P. R. Patel, H. Zhang, M. T. Robbins, J. B. Nofar, S. P. Marshall, M. J. Kobylarek, T. D. Y. Kozai, N. A. Kotov, C. A. Chestek, Chronic in vivo stability assessment of carbon fiber microelectrode arrays. *J. Neural Eng.* **13**, 066002 (2016).
23. W.-T. Tseng, C.-T. Yen, M.-L. Tsai, A bundled microwire array for long-term chronic single-unit recording in deep brain regions of behaving rats. *J. Neurosci. Methods* **201**, 368–376 (2011).
24. A. Zhukov, Design of the magnetic properties of fe-rich, glass-coated microwires for technical applications. *Adv. Funct. Mater.* **16**, 675–680 (2006).
25. S. A. Baranov, V. S. Larin, A. V. Torcunov, Technology, preparation and properties of the cast glass-coated magnetic microwires. *Crystals.* **7**, 136 (2017).
26. J. Foggiato, Chemical vapor deposition of silicon dioxie films, in *Handbook of Thin Film Deposition Processes and Techniques*, K. Seshan, Ed. (Elsevier, 2002), vol. 629.
27. J. P. Seymour, Y. M. Elkasabi, H.-Y. Chen, J. Lahann, D. R. Kipke, The insulation performance of reactive parylene films in implantable electronic devices. *Biomaterials* **30**, 6158–6167 (2009).

28. H.-C. Chang, L.-C. Wang, A simple proof of thue's theorem on circle packing. *Metric Geom.* 4 (2010).
29. A. M. Obaid, Y.-W. Wu, M.-E. Hanna, W. D. Nix, J. B. Ding, N. A. Melosh, Ultra-sensitive measurement of brain penetration with microscale probes for brain machine interface considerations. *bioRxiv*, 454520 (2018).
30. M. Fotino, Tip sharpening by normal and reverse electrochemical etching. *Rev. Sci. Instrum.* **64**, 159–167 (1993).
31. S. Awtar, A. Slocum, Flexure systems based on a symmetric diaphragm flexure, in *Proceedings of the ASPE 2005 Annual Meeting,* Norfolk, VA, Paper No. 1803 (2005).
32. A. Hierlemann, J. Muller, D. Bakkum, F. Franke, in *Technical Digest—International Electron Devices Meeting, IEDM* (2015), vol. 2016 February, pp. 13.2.1–13.2.4.
33. A. Cowley, B. Woodward, A healthy future: Platinum in medical applications. *Platin. Met. Rev.* **55**, 98–107 (2011).
34. C. Sekirnjak, P. Hottowy, A. Sher, W. Dabrowski, A. M. Litke, E. J. Chichilnisky, Electrical stimulation of mammalian retinal ganglion cells with multielectrode arrays. *J. Neurophysiol.* **95**, 3311–3327 (2006).
35. M. Fiscella, K. Farrow, I. L. Jones, D. Jäckel, J. Müller, U. Frey, D. J. Bakkum, P. Hantz, B. Roska, A. Hierlemann, Recording from defined populations of retinal ganglion cells using a high-density CMOS-integrated microelectrode array with real-time switchable electrode selection. *J. Neurosci. Methods* **211**, 103–113 (2012).
36. A. Drinnenberg, F. Franke, R. K. Morikawa, J. Jüttner, D. Hillier, P. Hantz, A. Hierlemann, R. Azeredo da Silveira, B. Roska, How diverse retinal functions arise from feedback at the first visual synapse. *Neuron* **99**, 117–134.e11 (2018).
37. J. E. Chung, J. F. Magland, A. H. Barnett, V. M. Tolosa, A. C. Tooker, K. Y. Lee, K. G. Shah, S. H. Felix, L. M. Frank, L. F. Greengard, A fully automated approach to spike sorting. *Neuron* **95**, 1381–1394.e6 (2017).
38. S. Venkatachalam, M. S. Fee, D. Kleinfeld, Ultra-miniature headstage with 6-channel drive and vacuum-assisted micro-wire implantation for chronic recording from the neocortex. *J. Neurosci. Methods* **90**, 37–46 (1999).
39. C. Bennett, S. Arroyo, S. Hestrin, Subthreshold mechanisms underlying state-dependent modulation of visual responses. *Neuron* **80**, 350–357 (2013).
40. E. V. Evarts, Relation of pyramidal tract activity to force exerted during voluntary movement. *J. Neurophysiol.* **31**, 14–27 (1968).
41. A. P. Georgopoulos, A. B. Schwartz, R. E. Kettner, Neuronal population coding of movement direction. *Science* **233**, 1416–1419 (1986).
42. D. W. Moran, A. B. Schwartz, Motor cortical representation of speed and direction during reaching. *J. Neurophysiol* **82**, 2676–2692 (1999).
43. P. Cisek, Preparing for speed. Focus on "Preparatory activity in premotor and motor cortex reflects the speed of the upcoming reach". *J. Neurophysiol.* **96**, 2842–2843 (2006).
44. H. Berger, Uber das Elektrenkephalogramm des Menschen. Zweite Mitteilung. *J. Psychol. Neurol. (Leipzig)* **40**, 160–179 (1930).
45. J. F. A. Poulet, C. C. H. Petersen, Internal brain state regulates membrane potential synchrony in barrel cortex of behaving mice. *Nature* **454**, 881–885 (2008).
46. G. Buzsáki, *Rhythms of the Brain* (Oxford Univ. Press, 2006).
47. E. Brazhnik, A. V. Cruz, I. Avila, M. I. Wahba, N. Novikov, N. M. Ilieva, A. J. McCoy, C. Gerber, J. R. Walters, State-dependent spike and local field synchronization between motor cortex and substantia nigra in hemiparkinsonian rats. *J. Neurosci.* **32**, 7869–7880 (2012).
48. H. G. Yamin, E. A. Stern, D. Cohen, Parallel processing of environmental recognition and locomotion in the mouse striatum. *J. Neurosci.* **33**, 473–484 (2013).
49. W. Yang, R. Yuste, In vivo imaging of neural activity. *Nat. Methods* **14**, 349–359 (2017).
50. J. G. Parker, J. D. Marshall, B. Ahanonu, Y.-W. Wu, T. H. Kim, B. F. Grewe, Y. Zhang, J. Z. Li, J. B. Ding, M. D. Ehlers, M. J. Schnitzer, Diametric neural ensemble dynamics in parkinsonian and dyskinetic states. *Nature* **557**, 177–182 (2018).
51. H. J. Gritton, W. M. Howe, M. F. Romano, A. G. DiFeliceantonio, M. A. Kramer, V. Saligrama, M. E. Bucklin, D. Zemel, X. Han, Unique contributions of parvalbumin and cholinergic interneurons in organizing striatal networks during movement. *Nat. Neurosci.* **22**, 586–597 (2019).
52. A. Zhou, B. C. Johnson, R. Muller, Toward true closed-loop neuromodulation: Artifact-free recording during stimulation. *Curr. Opin. Neurobiol.* **50**, 119–127 (2018).
53. V. Viswam, J. Dragas, A. Shadmani, Y. Chen, A. Stettler, J. Muller, A. Hierlemann, in *Digest of Technical Papers—IEEE International Solid-State Circuits Conference* (2016).
54. C. I. Dorta-Quiñones, M. Huang, J. C. Ruelas, J. Delacruz, A. B. Apsel, B. A. Minch, M. Lindau, A bidirectional-current CMOS potentiostat for fast-scan cyclic voltammetry detector arrays. *IEEE Trans. Biomed. Circuits Syst.* **12**, 894–903 (2018).
55. J. Dragas, V. Viswam, A. Shadmani, Y. Chen, R. Bounik, A. Stettler, M. Radivojevic, S. Geissler, M. E. J. Obien, J. Müller, A. Hierlemann, A multi-functional microelectrode array featuring 59 760 electrodes, 2048 electrophysiology channels, stimulation, impedance measurement, and neurotransmitter detection channels. *IEEE J. Solid-State Circuits* **52**, 1576–1590 (2017).
56. V. Viswam, D. Jäckel, I. Jones, M. Ballini, J. Muller, A. Stettler, U. Frey, F. Franke, A. Hierlemann, Effects of sub-10μm electrode sizes on extracellular recording of neuronal cells, in *18th International Conference on Miniaturized Systems for Chemistry and Life Sciences*, San Antonio, TX, USA, 26 to 30, October, 2014.
57. P. Hooylaerts, J. Bentell, J. Vermeiren, J. Neys, B. Grietens, M. O'Grady, T. Colin, Cheetah: A high frame rate, high resolution SWIR image camera. *Sensors, Systems, and Next-Generation Satellites XII* **7106**, 71061M (2008).
58. R. R. Racz, M. Kollo, G. Racz, C. Bulz, T. Ackels, T. Warner, W. Wray, N. Kiskin, C. Chen, Z. Ye, L. de Hoz, E. A. Rancz, A. T. Schaefer, jULIEs: Extracellular probes for recordings and stimulation in the structurally and functionally intact mouse brain. *bioRxiv*, 721548 (2019).
59. A. A. Robbins, S. E. Fox, G. L. Holmes, R. C. Scott, J. M. Barry, Short duration waveforms recorded extracellularly from freely moving rats are representative of axonal activity. *Front. Neural Circuits* **7**, 181 (2013).
60. D. J. Bakkum, U. Frey, D. Jäckel, M. E. J. Obien, A. Hierlemann, H. Takahashi, M. Radivojevic, The axon initial segment is the dominant contributor to the neuron's extracellular electrical potential landscape. *Adv. Biosyst.* **3**, 1800308 (2019).

Acknowledgments

Funding: Research at Stanford was supported by NIH BRAIN Initiative grant U01NS094248, NIH R21NS104861, NIH SBIR grant 5R43MH110287, DARPA's NESD program (contract number: N66001-17-C-4005), GG Technologies gift fund and the Wu Tsai Institute Big Ideas program; N.B. was supported by NSF GRFP DGE-114747 and NSF IGERT grant 0801700. This work was also supported by the Francis Crick Institute that receives its core funding from Cancer Research UK (FC001153), the UK Medical Research Council (FC001153), and the Wellcome Trust (FC001153); an HFSP grant to A.T.S. and N.A.M. (RGP 00048/2013); and the Medical Research Council (MC_UP_1202/5). The high-resolution CMOS-MEA chip and setup development was supported by the European Union through the H2020 ERC Advanced Grant "neuroXscales" (contract no. 694829); F.F. was supported by Swiss National Science Foundation Ambizione grant PZ00P3-167989. A.T.S. is a Wellcome Trust investigator (110174/Z/15/Z). **Author contributions:** The concept and design were initiated by A.O., M.-E.H., M.K., R.R., M.R.A., A.T.S., and N.A.M. Experiments and data acquisition were performed by A.O., M.-E.H., Y.-W.W., M.K., R.R., M.R.A., J.M., N.B., W.W., and F.F. Experimental design, interpretation of data, and analysis were performed by A.O., M.-E.H., Y.-W.W., M.K., R.R., M.R.A., J.M., N.B., W.W., F.F., E.J.C., A.H., J.B.D., A.T.S., and N.A.M. Writing was primarily performed by A.O., Y.-W.W., M.K., A.T.S., and N.A.M. **Competing interests:** M.R.A., A.T.S., and N.A.M. cofound and hold shares in Paradromics Inc., a company developing scalable electrophysiology. J.M. is a cofounder of MaxWell Biosystems AG. The following patents related to this work have been filed: US 14/937,740 (M.-E.H., M.R.A., J.B.D., A.T.S., and N.A.M.) and PCT/US2018/025576 (Y. Kong, M.R.A., M.E.H., A.O., and N.A.M.). All authors declare that they have no other competing interests. **Data and materials availability:** All data needed to evaluate the conclusions in the paper are present in the paper and/or the Supplementary Materials. Additional data related to this paper may be requested from the authors.

Submitted 5 June 2019
Accepted 26 December 2019
Published 20 March 2020
10.1126/sciadv.aay2789

Citation: A. Obaid, M.-E. Hanna, Y.-W. Wu, M. Kollo, R. Racz, M. R. Angle, J. Müller, N. Brackbill, W. Wray, F. Franke, E. J. Chichilnisky, A. Hierlemann, J. B. Ding, A. T. Schaefer, N. A. Melosh, Massively parallel microwire arrays integrated with CMOS chips for neural recording. *Sci. Adv.* **6**, eaay2789 (2020).